Environmental Science: Atmospheres

ROYAL SOCIETY OF CHEMISTRY

PAPER

View Article Online
View Journal | View Issue

Cite this: *Environ. Sci.: Atmos.*, 2022, **2**, 1023

Geometries, molecular Rayleigh scattering, Raman and infrared frequencies of polycyclic aromatic hydrocarbons and subunits of graphite studied by DFT methods†

Freja Hasager, Ole John Nielsen and Kurt V. Mikkelsen *

Received 20th December 2021
Accepted 20th July 2022

DOI: 10.1039/d1ea00105a

rsc.li/esatmospheres

This study presents a computational investigation of geometric parameters, infrared (IR) and Raman frequencies as well as molecular Rayleigh scattering of polycyclic aromatic hydrocarbons (PAHs), used as models for subunits of larger graphitic materials. DFT functionals B3LYP, ωB97XD and M06-2X with basis sets 6-31+G(d,p), 6-311+G(d,p), aug-cc-pVDZ and aug-cc-pVTZ were utilized in different combinations in the investigation of two molecular systems: 2*H*-benzo(*cd*)pyrene and double-layered 2*H*-benzo(*cd*)pyrene. Bond lengths and angles of central carbon atoms in the different subunits varied by a maximum of 2% between systems. Calculated Raman spectra compare well with experimental and simulated Raman spectra from the literature of other PAHs, and only to some extent with experimental spectra of graphitic materials. The molecular Rayleigh scattering was found to increase by a factor of 3.5 upon addition of an extra layer to the system.

Environmental significance

We investigate how black carbon particles can affect the climate by the direct scattering and absorption of light. Black carbon (BC) particles are strong warming agents of the same magnitude as methane and they pose a threat to human health. Emissions of these particles are estimated to be around 7500 Gg year^{-1} and the particles are able to travel long distances from the source areas. Basically, BC particles are systems that we need to know more about. It is important to know the photophysical properties of the BC particles in order to understand their impact on the climate.

1 Introduction

Aerosols affect climate by the direct scattering and absorption of light and by the indirect effect of cloud interactions.[1,2] Carbonaceous particles pose a threat to human health as they have been found to be the cause of cardiovascular and respiratory diseases.[3,4] Ultrafine BC particles (less than 0.1 μm) and fine (less than 2.5 μm) penetrate deep into the lungs and carry with them carcinogenic polycyclic aromatic hydrocarbons causing lung cancer.[3,4,5] Black carbon (BC) is a strong warming agent of the same magnitude as methane.[6] The source of BC is incomplete fossil fuel combustion and biomass burning. The term soot is used mainly in the combustion community whereas BC is used in the atmospheric community. Different emission inventory methods estimated the 2000 total global BC emissions to be 7500 Gg year^{-1} with an uncertainty of 2000–29,000 Gg year^{-1}.[7] There is a large potential for emission reductions. BC also plays a special positive warming role in the Arctic due to deposition on snow and ice. It is well known that BC particles travel long distances from the source areas.[8,9] BC particles are spherules consisting of wrinkled graphite layers forming disordered structures containing different levels of elemental carbon and they absorb strongly in the ultraviolet, visible and infrared wavelength ranges. Measurements of BC mass concentrations rely on the optical properties of BC. Real-time methods are based on measurements of optical properties: extinction, scattering and absorption in wavelength regions where interferences from other species can be minimized or completely avoided. Large uncertainties exist in the determination of aerosol induced radiative forcing used in climate models.[6] Assessment of the properties of particles is thus important in understanding the climate impact of anthropogenic aerosol emissions, and hence minimizing the uncertainty in the radiative forcing from aerosols in climate models. Optical properties are also important for detection and quantification of BC. In this study graphite subunits were used to investigate properties of graphite on the molecular scale. Here, the vibrational frequencies, Raman shifts and Rayleigh scattering, as well as the geometries have been determined for two different polycyclic aromatic hydrocarbons. The

Department of Chemistry, University of Copenhagen, Universitetsparken 5, 2100 Copenhagen Ø, Denmark. E-mail: kmi@chem.ku.dk

† Electronic supplementary information (ESI) available. See https://doi.org/10.1039/d1ea00105a

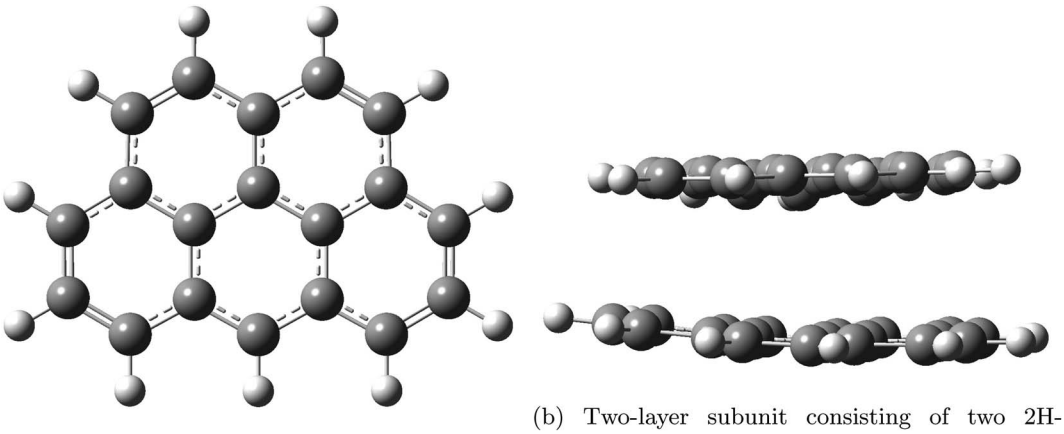

(a) 2H-Benzo(cd)pyrene. (b) Two-layer subunit consisting of two 2H-benzo(cd)pyrene molecules.

Fig. 1 Graphite subunits investigated in this study: 2*H*-benzo(*cd*)pyrene (a) and double-layer 2*H* benzo(*cd*)pyrene (b). Gray represents carbon atoms and white represents hydrogen atoms.

investigated subunits were: 2*H*-benzo(*cd*)pyrene and a double-layer system consisting of two 2*H*-benzo(*cd*)pyrene molecules. The structures are given in Fig. 1.

2 Computational approach

Graphite subunits were investigated computationally using the Gaussian16 program.[10] Calculations were performed with three density functional theory (DFT) functionals: B3LYP, ωB97XD and M06-2X. The hybrid functional B3LYP was chosen, as it has previously proven useful in the study of PAHs.[11,12] The ωB97XD functional has also shown to provide reliable results for PAHs[13] and the Minnesota functional M06-2X has previously given excellent results for aromatic–aromatic stacking interactions.[14] The DFT functionals were used in combination with the basis sets 6-31+G(d,p) and 6-311+G(d,p)[15] and the correlation consistent basis sets aug-cc-pVDZ and aug-cc-pVTZ.[16] Specifically, 2*H*-benzo(*cd*)pyrene was investigated using B3LYP, ωB97XD and M06-2X in combination with 6-31+G(d,p), 6-311+G(d,p), aug-cc-pVDZ, and aug-cc-pVTZ, while the double-layer subunit was investigated using B3LYP, ωB97XD and M06-2X in combination with basis sets 6-31+G(d,p) and 6-311+G(d,p). As this study presumes to model graphite subunits, diffuse functions were added only to the carbon atoms. Polarization functions were added to both hydrogen and carbon atoms.

Isotropic, α, and anisotropic, β, polarizabilities were used to calculate the molecular Rayleigh scattering $\langle R \rangle$ by the relation $\langle R \rangle = 45\alpha^2 + 13\beta^2$.[17,18]

3 Results and discussion

3.1 Geometry optimizations

3.1.1 Single-layer subunit. Geometry optimizations of 2*H*-benzo(*cd*)pyrene were performed at the B3LYP, ωB97XD, and M06-2X levels with the basis sets 6-31+G(d,p), 6-311+G(d,p) and aug-cc-pVDZ. The basis set aug-cc-pVTZ was also used with functionals B3LYP and M06-2X (Fig. 2). The three carbon atoms in the center of the molecule, 3, 4 and 8, were investigated with respect to bond lengths, denoted *R*, and bond angle, denoted *A*. The bond lengths and the bond angles calculated at different levels of theory are represented in Fig. 3. Values used to construct the plot, as well as all following plots, can be found in the ESI.† The bond lengths *R*(3, 4) and *R*(3, 8) proved to be identical within the same method/basis set combination. Variation between method/basis set are greatest between the B3LYP/aug-cc-pVDZ and M06-2X/aug-cc-pVTZ calculations with a variation of 0.6%. The largest variation of the bond angle is between the B3LYP/6-31+G(d,p) and M06-2X/6-311+G(d,p) calculations with a value of 0.1%. Thus, the geometry does not change notably between the different levels of computational method.

3.1.2 Double-layer subunit. Geometry optimizations for the double-layer graphite subunit, consisting of two 2*H*-benzo(*cd*)pyrene molecules, were performed utilizing B3LYP, ωB97XD and M06-2X functionals with 6-31+G(d,p) and 6-311+G(d,p)

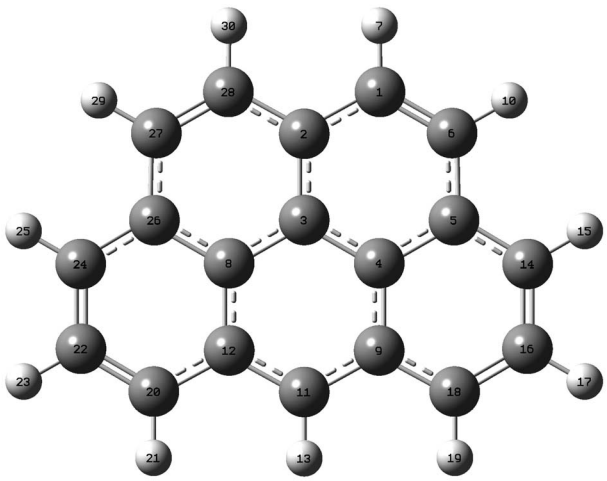

Fig. 2 2*H*-Benzo(*cd*)pyrene optimized at the M06-2X/aug-cc-pVTZ level of theory. Labels indicate atom number.

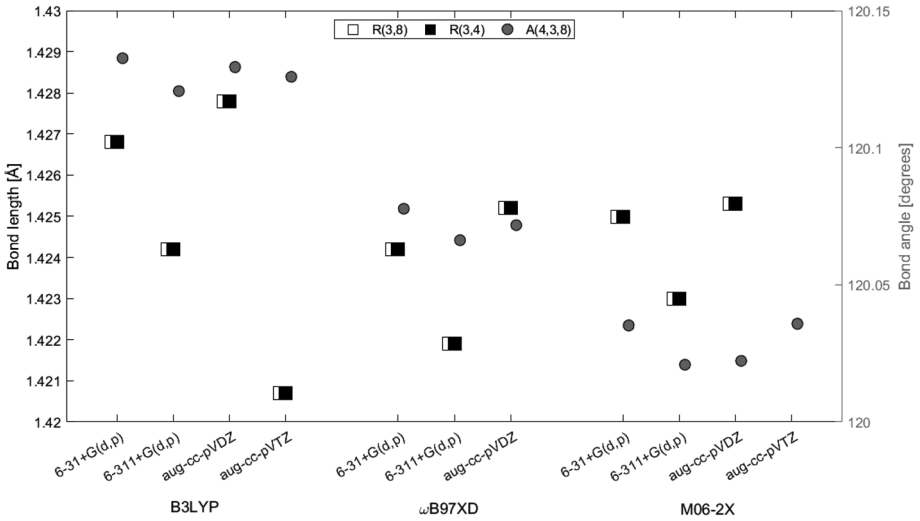

Fig. 3 Bond lengths of *R*(3, 4) (white squares), *R*(3, 8) (black squares) and angle *A*(4, 3, 8) (gray circle) between center atoms of 2*H*-benzo(*cd*) pyrene as a function of method and basis set. Bond lengths are given on the left axis and the bond angle is given on the right axis.

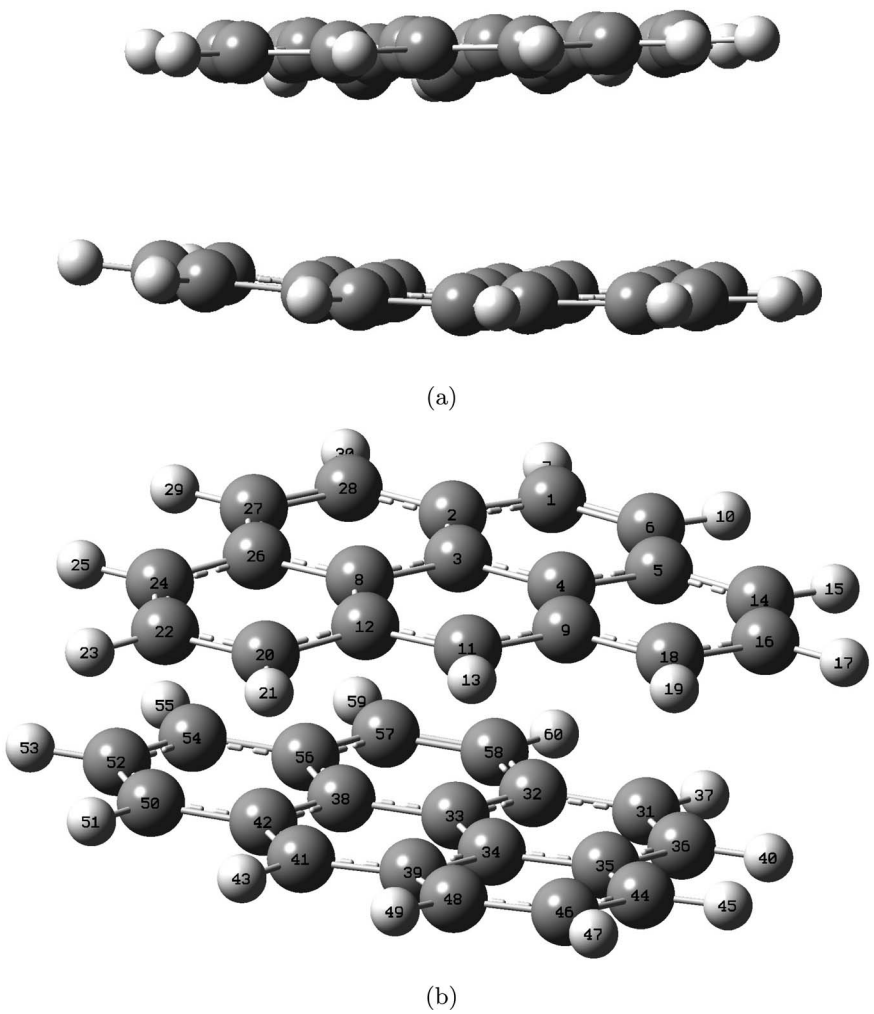

Fig. 4 Structure of the double-layered graphite subunit optimized at the M06-2X/6-311+G(d,p) level, shown from side view (a) and top-side view (b). Labels indicate atom number.

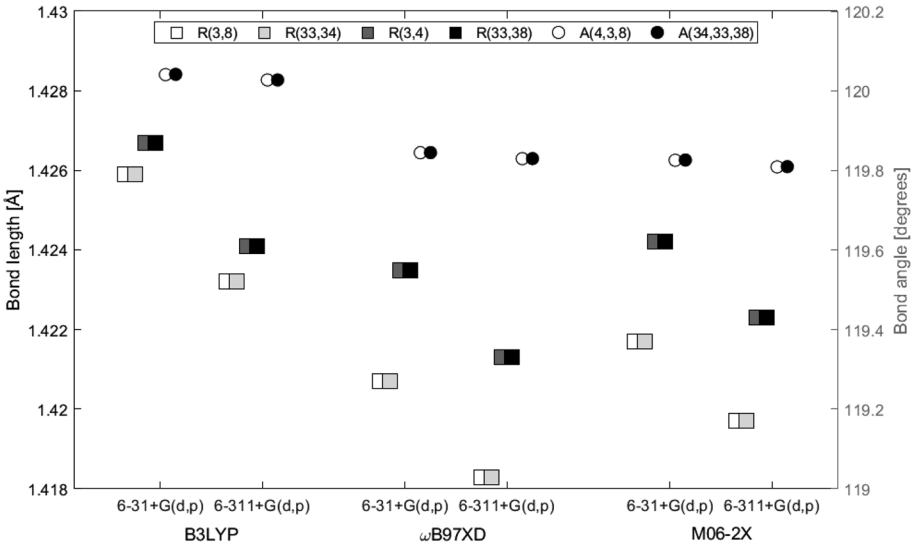

Fig. 5 Bond lengths and angles of center atoms of the double-layer structure as a function of functional and basis set. Squares represent bond lengths and are given on the left axis. Circles represent bond angles and are given on the right axis.

basis sets. Fig. 4 displays an optimized structure of the double-layered subunit from two different angles.

The distance between the two layers, 3.3222 Å, is estimated in GaussView6.0.16 (ref. 19) as the distance between atom 3 and 33, both located at the center in each of the two layers. In Fig. 5 the bond lengths and angles between the center atoms in the two layers are shown as a function of basis set and method. The 6-31+G(d,p) basis set systematically estimates higher values

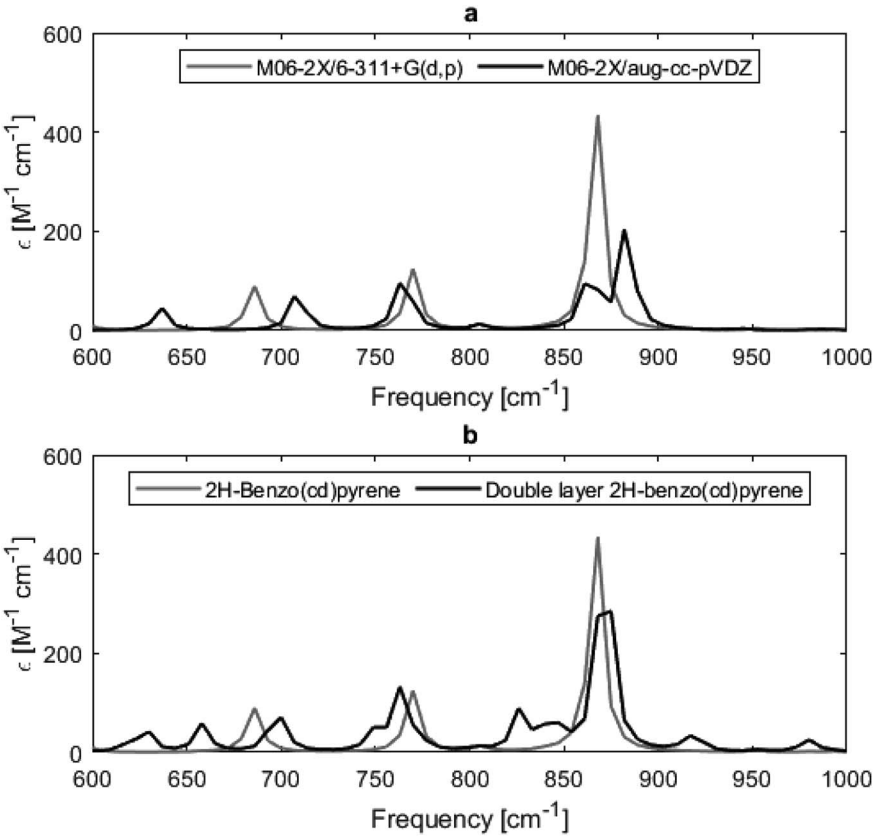

Fig. 6 Calculated IR spectra of 2*H*-benzo(*cd*)pyrene at the M06-2X/6-311+G(d,p) and M06-2X/aug-cc-pVDZ level of theory (a), and of 2*H*-benzo(*cd*)pyrene and double-layered 2*H*-benzo(*cd*)pyrene at the M06-2X/6-311+G(d,p) level of theory (b).

Table 1 Vibrational IR frequencies in units of cm^{-1} of the major peak for 2*H*-benzo(*cd*)pyrene and double-layer 2*H*-benzo(*cd*)pyrene

	B3LYP	ωB97XD	M06-2X
2*H*-Benzo(*cd*)pyrene			
6-31+G(d,p)	860.5708	869.8538	871.9956
6-311+G(d,p)	857.9248	866.3583	867.063
aug-cc-pVDZ	870.8079	878.762	883.4537
Double-layer			
6-31+G(d,p)	865.2546	880.3031	877.3855
6-311+G(d,p)	858.5925	871.9908	873.8561

than 6-311+G(d,p) by a maximum of 0.2%. Bond lengths *R*(3, 4), *R*(3, 8) and angle *A*(4, 3, 8) belong to the top layer, while bond lengths *R*(33, 34), *R*(33, 38) and angle *A*(34, 33, 38) belong to the bottom layer. The two angles are almost identical at a given functional/basis set combination. Angles obtained by different combinations of basis set and functional only vary up to 0.2%. The greatest variation between bond lengths, regardless of basis set/functional combination, proved to be 0.6%. As for the single layer, only small variations in the optimized geometries were identified depending on level of theory and/or location in the system.

3.2 Spectral properties

IR vibrational frequencies, Raman shifts and polarizabilities were calculated for 2*H*-benzo(*cd*)pyrene utilizing functionals B3LYP, ωB97XD and M06-2X with basis sets 6-31+G(d,p), 6-311+G(d,p) and aug-cc-pVDZ. For the double-layer subunit, functionals B3LYP, ωB97XD, and M06-2X were utilized in combination with basis sets 6-31+G(d,p) and 6-311+G(d,p).

3.2.1 Infrared frequencies. Experimentally determined IR spectra of graphite crystallites, carbon nanotubes and highly oriented pyrolytic carbon show two major active modes at 868 cm^{-1} and 1575 cm^{-1}, from out-of-plane and in-plane carbon–carbon vibrations, respectively.[20] The calculated IR spectra of 2*H*-benzo(*cd*)pyrene and the double-layer subunit are given in Fig. 6b, and show one dominant peak in the 850–900 cm^{-1} range that corresponds to the out-of-plane C–C vibrational mode. The double-layer subunit also has a C–H vibrational mode at 3200 cm^{-1}. The peak at 1575 cm^{-1} is only of minor intensity in the theoretical spectra. Possibly due to the model systems being much smaller than the measured system, *i.e.* the model systems contain fewer C–C bonds that can contribute to the intensity of the 1575 cm^{-1} peak. Likewise, the experimental spectra do not contain a peak at 3200 cm^{-1}, as there are zero to little C–H bonds in the system. It is also seen that the spectrum of the double-layer subunit contains more IR features than the spectrum of 2*H*-benzo(*cd*)pyrene, as the extra layer introduces more vibrational modes.

The calculated IR spectra of 2*H*-benzo(*cd*)pyrene and the double-layer subunit contain major peaks in the 850–900 cm^{-1} range arising from the out-of-plane vibration. Thus this mode has been compared to the experimental value of 868 cm^{-1}. Improved computational accuracy would be expected as a result of increasing basis set size and with each step up on the rungs of Jacob's ladder.[21,22] In Table 1 and Fig. 7 it is seen that the frequency for 2*H*-benzo(*cd*)pyrene calculated at the M06-2X/6-311+G(d,p) level is closest to the experimental value, underestimating the experimental frequency by 1 cm^{-1}. The calculations from ωB97XD in combination with the Pople basis sets are 2 cm^{-1} from the experimental value, and hence the second best determinations. The ωB97XD and M06-2X with aug-cc-pVDZ levels overestimate the frequency by 11 and 15 cm^{-1},

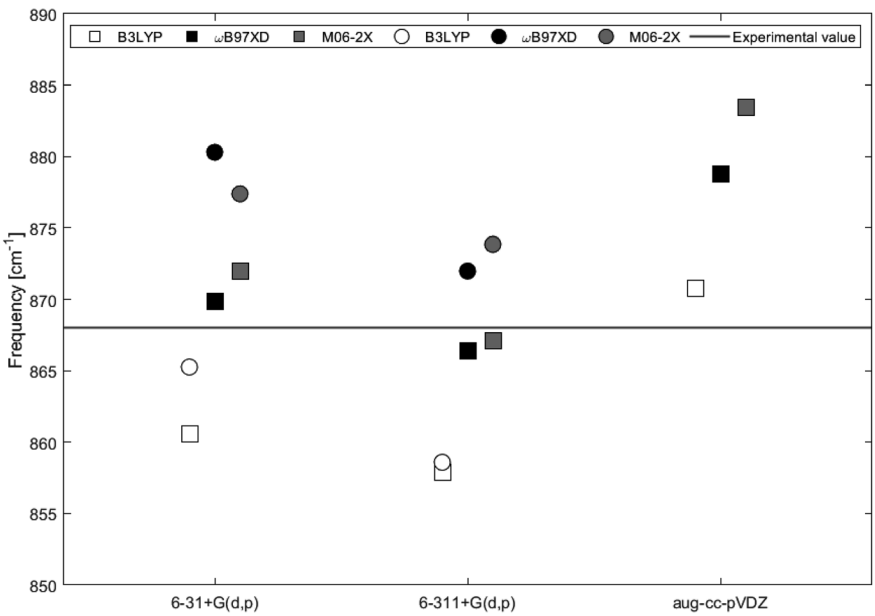

Fig. 7 IR vibrational frequencies of the major peak for 2*H*-benzo(*cd*)pyrene (squares) and the double-layer subunit (circles) obtained by different levels of theory. The black line represents the experimental value of 868 cm^{-1} from Kastner *et al.*[20]

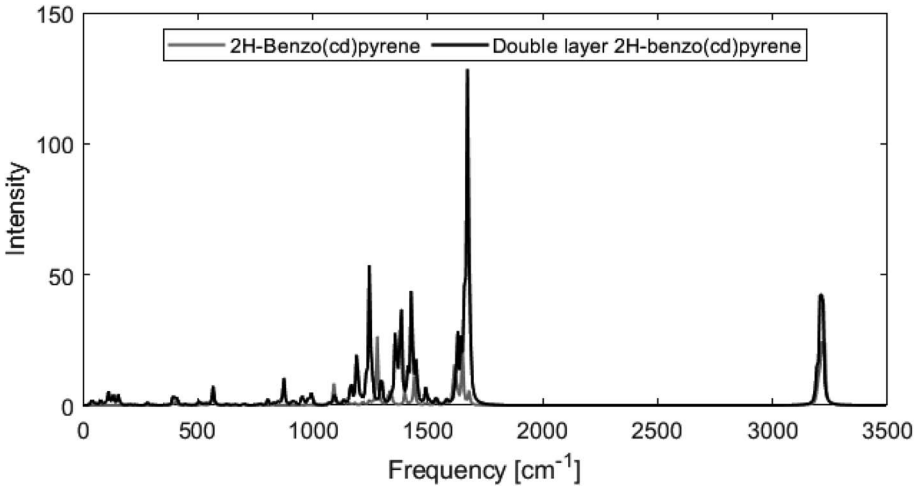

Fig. 8 Raman spectra obtained from M06-2X/6-311+G(d,p) calculations of 2*H*-benzo(*cd*)pyrene (gray line) and the double-layer subunit (black line).

respectively, while the B3LYP/aug-cc-pVDZ level yields a value 3 cm^{-1} above the experimental. The B3LYP method combined with 6-31+G(d,p) and 6-311+G(d,p) underestimates the frequency by 7 and 10 cm^{-1}, respectively. The IR spectra of 2*H*-benzo(*cd*)pyrene calculated at the aug-cc-pVDZ level show that the peak in the 850–900 cm^{-1} range is split in two, whereas the other basis sets yield spectra with only one peak in that range, see Fig. 6a. The peak used for the aug-cc-pVDZ analysis is the high energy split, which is a possible explanation for why aug-cc-pVDZ overestimates the frequency. For the double-layer 2*H*-benzo(*cd*)pyrene the aug-cc-pVDZ basis set was not utilized. The B3LYP calculations underestimate the frequency by 3 cm^{-1} and 9 cm^{-1} for 6-31+G(d,p) and 6-311+G(d,p), respectively. Hence, the B3LYP/6-31+G(d,p) method yields the best value. Functionals ωB97XD and M06-2X with the basis set 6-31+G(d,p) overestimate the frequency by 12 cm^{-1} and 9 cm^{-1}, respectively, while the ωB97XD/6-311+G(d,p) and M06-2X/6-311+G(d,p) calculations overestimate the frequency by 4 cm^{-1} and 6 cm^{-1}, respectively.

On the basis of this investigation it is concluded that the ωB97XD/6-311+G(d,p) level of theory yields reliable results for both 2*H*-benzo(*cd*)pyrene and double-layered 2*H*-benzo(*cd*)pyrene, with a maximum variation of 0.5% from the experimental value. It is expected that by increasing the size of the subunit a better calculated value would be obtained, as the graphitic material used for the experimental determination is a large

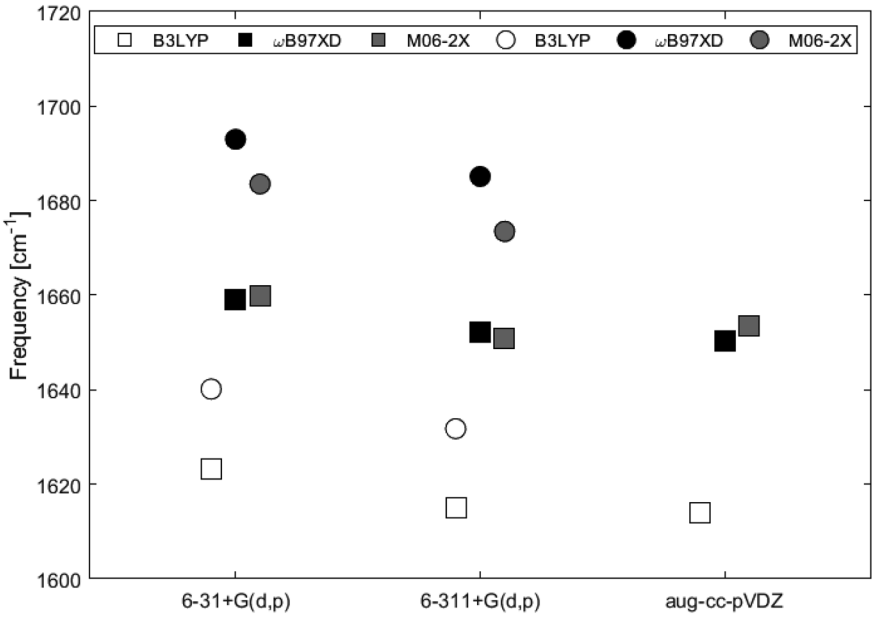

Fig. 9 Major Raman shifts in the 1600–1700 cm^{-1} range calculated at different levels of theory for 2*H*-benzo(*cd*)pyrene (squares) and the double-layer subunit (circles).

Table 2 Raman shifts given in units of cm^{-1} of the major peak for 2*H*-benzo(*cd*)pyrene and double-layer 2*H*-benzo(*cd*)pyrene calculated at different levels of theory

	B3LYP	ωB97XD	M06-2X
2*H*-Benzo(*cd*)pyrene			
6-31+G(d,p)	1623.2125	1659.0021	1659.7803
6-311+G(d,p)	1615.0978	1652.0413	1650.9097
aug-cc-pVDZ	1614.0553	1650.3219	1653.6153
Double-layer			
6-31+G(d,p)	1640.1342	1692.9805	1683.5198
6-311+G(d,p)	1631.7723	1685.1069	1673.4912

Table 3 Isotropic and anisotropic polarizabilities of 2*H*-benzo(*cd*)pyrene and the double-layer subunit given in atomic units

	Isotropic			Anisotropic		
	B3LYP	ωB97XD	M06-2X	B3LYP	ωB97XD	M06-2X
2*H*-Benzo(*cd*)pyrene						
6-31+G(d,p)	244.92	234.42	239.05	230.02	214.86	225.31
6-311+G(d,p)	243.80	234.33	237.03	228.85	214.33	221.21
aug-cc-pVDZ	252.18	243.25	246.25	232.09	216.72	225.72
Double-layer						
6-31+G(d,p)	537.34	481.81	481.03	164.12	162.58	171.98
6-311+G(d,p)	528.23	480.39	476.89	159.46	162.20	169.57

multi-layer system. Comparison between the two subunits relative to the experimental value were done for frequencies obtained by B3LYP, ωB97XD and M06-2X with basis sets 6-31+G(d,p) and 6-311+G(d,p). The calculated value for 2*H*-benzo(*cd*)pyrene maximally varies 1.2% from the experimental value, and 1.4% for double-layered 2*H*-benzo(*cd*)pyrene. Hence, no improvement was observed going from the single to the double-layer subunit. It is important to note that the experimental IR features were measured for graphitic systems much larger than the two subunits investigated here. Additionally, calculations were performed for vacuum conditions, while experiments were not conducted in vacuum. This introduces some uncertainty when comparing theoretical and experimental values, as these may not be directly comparable.

3.2.2 Raman shifts. Experimental Raman spectra of graphitic materials show an intense peak at 1580–1583 cm^{-1} and another at 1350–1370 cm^{-1}.[20,23,24] The 1580–1583 cm^{-1} peak, called the G band, arises from sp^2 carbon in the crystalline part of graphite, and the 1350–1370 cm^{-1} peak, named the D band, arises from defects in the crystalline part, like the edge-line. Experimental Raman spectra also contain two overtone features: D′ at 1620 cm^{-1} and G′ at around 2700 cm^{-1}.[25] The G′ band broadens with increasing number of layers.[26]

Fig. 8 shows calculated Raman spectra for 2*H*-benzo(*cd*)pyrene and the double-layer system calculated at the M06-2X/6-311+G(d,p) level. Very notable is the "missing" G′ band at 2700 cm^{-1} characteristic for graphitic materials. For both subunits, the spectra contain features at around 1240–1280 cm^{-1} and 1650–1670 cm^{-1} that could be associated with the D band from sp^2 carbon and the G band from disorder. At around 3200 cm^{-1} the calculated spectra each have a medium/strong peak that arises from the C–H modes, similar to what is observed for various PAHs.[11,27] The Raman spectra of these PAHs contain several features in the 1000–1500 cm^{-1} range.

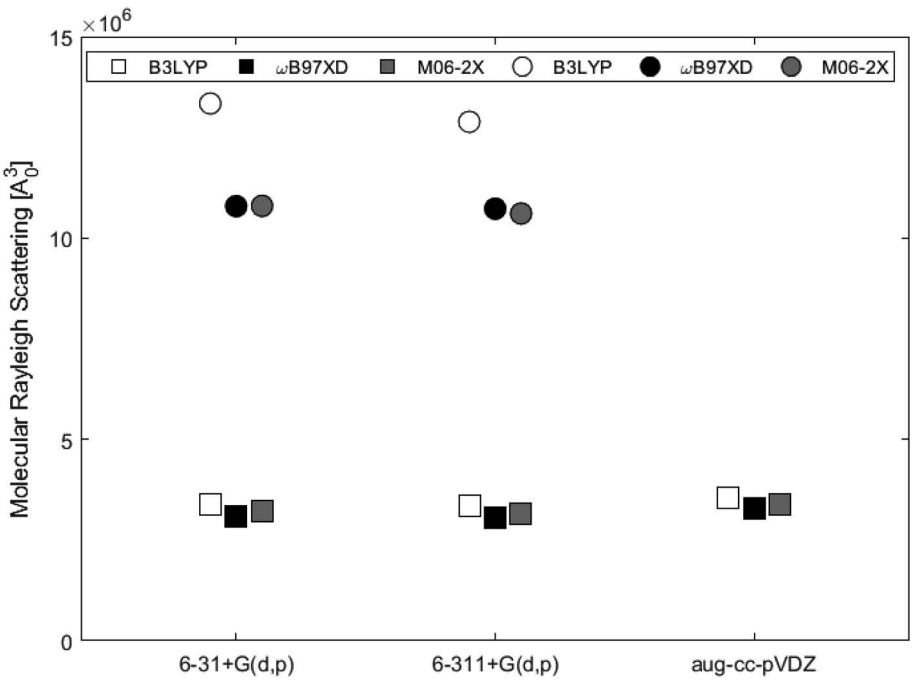

Fig. 10 Molecular Rayleigh scattering for 2*H*-benzo(*cd*)pyrene (squares) and the double-layer subunit (circles) obtained from different levels of theory.

Thus, the Raman features identified here resemble PAHs better than they resemble graphite.

From Fig. 8 it is evident that the calculated Raman spectra for 2*H*-benzo(*cd*)pyrene and the double-layer subunit look somewhat similar. The features in the double-layer spectrum are shifted a bit to the left relative to the spectrum of 2*H*-benzo(*cd*)pyrene. Both spectra contain several peaks in the 1100–1600 cm^{-1} range. A zoom of this range, see ESI,† shows that the double-layer subunit spectrum contains more features than the 2*H*-benzo(*cd*)pyrene spectrum, which is not surprising, as larger systems contain more vibrational modes.

Fig. 9 and Table 2 show the Raman shifts at ~1600–1700 cm^{-1} arising from the C–C in-plane vibrational mode, for 2*H*-benzo(*cd*)pyrene and the double-layer subunit calculated at different levels of theory. Comparison of the shifts within the same functional but varying basis set yields a maximum variation of 1% for each of the two subunits. Comparison of the shifts between the two subunits calculated utilizing all functionals with basis sets 6-31+G(d,p) and 6-311+G(d,p) yields a maximum variation of 2% for the ωB97XD/6-31+G(d,p) determinations, and a minimum variation of 1% for the B3LYP/6-311+G(d,p) determinations. Functionals ωB97XD and M06-2X yield similar results for each of the subunits, while values calculated at the B3LYP level are generally lower.

3.2.3 Rayleigh scattering. Table 3 shows the isotropic and anisotropic polarizabilities of the two subunits calculated at the different levels of theory. These polarizabilities are used to calculate the molecular Rayleigh scattering presented in Fig. 10. The average value for 2*H*-benzo(*cd*)pyrene was $3.23 \times 10^6\ a_0^3$, while the average value for the double-layer subunit was $1.15 \times 10^7\ a_0^3$, *i.e.* a factor of 3.5 larger. This agrees well with the fact that larger species scatter more light. B3LYP estimates higher scattering than ωB97XD and M06-2X by about 10% for 2*H*-benzo(*cd*)pyrene and about 20% for the double-layer subunit.

4 Conclusion

DFT functionals combined with different basis sets have been used to investigate geometries, IR vibrational frequencies, Raman shifts and molecular Rayleigh scattering for two molecular systems used as model units for graphite. Geometry parameters of 2*H*-benzo(*cd*)pyrene were calculated using DFT functionals B3LYP, ωB97XD, M06-2X in combination with basis sets 6-31+G(d,p), 6-311+G(d,p) and aug-cc-pVDZ. Functionals B3LYP and M06-2X with basis set aug-cc-pVTZ were also utilized for the geometry optimization of 2*H*-benzo(*cd*)pyrene. The geometry of double-layered 2*H*-benzo(*cd*)pyrene was calculated utilizing functionals B3LYP, ωB97XD, M06-2X with basis sets 6-31+G(d,p) and 6-311+G(d,p). Bond lengths and bond angles of central atoms in the two systems proved to vary by less than 2% and 0.1%, respectively, between the systems. Thus, the configurations of atoms in these systems are not greatly affected by increasing the system size by addition of an extra layer.

Theoretical IR spectra were calculated for both subunits. The functionals B3LYP, ωB97XD, M06-2X with the basis sets 6-31+G(d,p), 6-311+G(d,p) and aug-cc-pVDZ was used for 2*H*-benzo(*cd*)pyrene, while the basis sets 6-31+G(d,p) and 6-311+G(d,p) were utilized for the double-layer structure. IR spectra contained a prominent peak at ~850–900 cm^{-1}, arising from out-of-plane C–C vibrations. Comparison of this vibrational frequency with an experimental value of 868 cm^{-1} for graphitic material showed no improvement of accuracy by the addition of an extra layer of 2*H*-benzo(*cd*)pyrene to the system. It was also found that the ωB97XD/6-311+G(d,p) level of theory yields the best result for both the single- and double-layer subunits.

Calculated Raman spectra of the two subunits compared better with experimental Raman spectra of PAHs than to those of graphitic materials. Raman shifts of the C–C in-plane vibrational mode calculated using B3LYP, ωB97XD and M06-2X with basis sets 6-31+G(d,p) and 6-311+G(d,p), varied up to 1% between basis sets within a given functional for each of the two subunits, and up to 2% for comparison of the two systems within same functional/basis set combination. The most consistent results were obtained by ωB97XD and M06-2X.

Isotropic and anisotropic polarizabilities were calculated and used to determine molecular Rayleigh scattering. Evaluation of the scattering obtained from the B3LYP, ωB97XD and M06-2X functionals with basis sets 6-31+G(d,p) and 6-311+G(d,p) for the two systems, showed that ωB97XD and M06-2X yielded similar results for each of the systems, while B3LYP estimated values about 10% and 20% higher for the single- and double-layer subunits, respectively.

In summary, it has been found that the computational methods ωB97XD, M06-2X/6-31+G(d,p), 6-311+G(d,p) are useful tools for theoretical investigations of large polycyclic aromatic hydrocarbons and consequently useful in expanding our understanding of graphitic materials on the molecular scale.

Conflicts of interest

There are no conflicts to declare.

References

1 J. Haywood and O. Boucher, *Rev. Geophys.*, 2000, **38**, 513–543.
2 J. Fan, Y. Wang, D. Rosenfeld and X. Liu, *J. Atmos. Sci.*, 2016, **73**, 4221–4252.
3 P. M. Mannucci, S. Harari, I. Martinelli and M. Franchini, *Internal and Emergency Medicine*, 2015, **10**, 657–662.
4 J. S. Lighty, J. M. Veranth and A. F. Sarofim, *J. Air Waste Manage. Assoc.*, 2000, **50**, 1565–1618.
5 A. A. Koelmans, M. T. Jonker, G. Cornelissen, T. D. Bucheli, P. C. Van Noort and Ö. Gustafsson, *Chemosphere*, 2006, **63**, 365–377.
6 G. Myhre, D. Shindell, F.-M. Bréon, W. Collins, J. Fuglestvedt, J. Huang, D. Koch, J.-F. Lamarque, D. Lee, B. Mendoza, T. Nakajima, A. Robock, G. Stephens, T. Takemura and H. Zhang, in *Anthropogenic and Natural Radiative Forcing*, ed. T. Stocker, D. Qin, G.-K. Plattner, M. Tignor, S. Allen, J. Boschung, A. Nauels, Y. Xia, V. Bex and P. Midgley, Cambridge University Press, Cambridge, United Kingdom and New York, NY, USA, 2013, book section 8, pp. 659–740.

7 T. C. Bond, S. J. Doherty, D. W. Fahey, P. M. Forster, T. Berntsen, B. J. DeAngelo, M. G. Flanner, S. Ghan, B. Kärcher, D. Koch, *et al.*, *J. Geophys. Res.: Atmos.*, 2013, **118**, 5380–5552.
8 E. Freud, R. Krejci, P. Tunved, R. Leaitch, Q. T. Nguyen, A. Massling, H. Skov and L. Barrie, *Atmos. Chem. Phys.*, 2017, **17**, 8101–8128.
9 K. S. Law and A. Stohl, *Science*, 2007, **315**, 1537–1540.
10 M. J. Frisch, G. W. Trucks, H. B. Schlegel, G. E. Scuseria, M. A. Robb, J. R. Cheeseman, G. Scalmani, V. Barone, G. A. Petersson, H. Nakatsuji, X. Li, M. Caricato, A. V. Marenich, J. Bloino, B. G. Janesko, R. Gomperts, B. Mennucci, H. P. Hratchian, J. V. Ortiz, A. F. Izmaylov, J. L. Sonnenberg, D. Williams-Young, F. Ding, F. Lipparini, F. Egidi, J. Goings, B. Peng, A. Petrone, T. Henderson, D. Ranasinghe, V. G. Zakrzewski, J. Gao, N. Rega, G. Zheng, W. Liang, M. Hada, M. Ehara, K. Toyota, R. Fukuda, J. Hasegawa, M. Ishida, T. Nakajima, Y. Honda, O. Kitao, H. Nakai, T. Vreven, K. Throssell, J. A. Montgomery Jr, J. E. Peralta, F. Ogliaro, M. J. Bearpark, J. J. Heyd, E. N. Brothers, K. N. Kudin, V. N. Staroverov, T. A. Keith, R. Kobayashi, J. Normand, K. Raghavachari, A. P. Rendell, J. C. Burant, S. S. Iyengar, J. Tomasi, M. Cossi, J. M. Millam, M. Klene, C. Adamo, R. Cammi, J. W. Ochterski, R. L. Martin, K. Morokuma, O. Farkas, J. B. Foresman and D. J. Fox, *Gaussian~16 Revision C.01*, Gaussian Inc., Wallingford CT, 2016.
11 F. Negri, C. Castiglioni, M. Tommasini and G. Zerbi, *J. Phys. Chem. A*, 2002, **106**, 3306–3317.
12 D. G. Smith and K. Patkowski, *J. Chem. Theory Comput.*, 2012, **9**, 370–389.
13 A. Yadav and P. Mishra, *Mol. Phys.*, 2014, **112**, 88–96.
14 Y. Zhao and D. G. Truhlar, *Acc. Chem. Res.*, 2008, **41**, 157–167.
15 M. J. Frisch, J. A. Pople and J. S. Binkley, *J. Chem. Phys.*, 1984, **80**, 3265–3269.
16 T. H. Dunning Jr, *J. Chem. Phys.*, 1989, **90**, 1007–1023.
17 T. Joranger, J. V. Kildgaard, S. Jørgensen, J. Elm and K. V. Mikkelsen, *Phys. Chem. Chem. Phys.*, 2019, **21**, 17274–17287.
18 J. Elm, P. Norman, M. Bilde and K. V. Mikkelsen, *Phys. Chem. Chem. Phys.*, 2014, **16**, 10883–10890.
19 R. Dennington, T. A. Keith and J. M. Millam, *GaussView Version 6*, Semichem Inc., Shawnee Mission KS, 2019.
20 J. Kastner, T. Pichler, H. Kuzmany, S. Curran, W. Blau, D. Weldon, M. Delamesiere, S. Draper and H. Zandbergen, *Chem. Phys. Lett.*, 1994, **221**, 53–58.
21 S. Kurth, J. P. Perdew and P. Blaha, *Int. J. Quantum Chem.*, 1999, **75**, 889–909.
22 J. P. Perdew, A. Ruzsinszky, J. Tao, V. N. Staroverov, G. E. Scuseria and G. I. Csonka, *J. Chem. Phys.*, 2005, **123**, 062201.
23 S. Reich and C. Thomsen, *Philos. Trans. R. Soc., A*, 2004, **362**, 2271–2288.
24 R. Vidano, D. Fischbach, L. Willis and T. Loehr, *Solid State Commun.*, 1981, **39**, 341–344.
25 M. Pimenta, G. Dresselhaus, M. S. Dresselhaus, L. Cancado, A. Jorio and R. Saito, *Phys. Chem. Chem. Phys.*, 2007, **9**, 1276–1290.
26 S. Reichardt and L. Wirtz, *Optical Properties of Graphene*, World Scientific, 2017, pp. 85–132.
27 W. Maddams and I. Royaud, *Spectrochim. Acta, Part A*, 1990, **46**, 309–314.